chemosensors

MDPI

Article

An IL/c-MWCNTs@Cu-ZIF-67-Modified Electrochemical Sensor for the Individual Determination of Bisphenol A and Bisphenol S in Plastic Leachates

Jing Xu [1], Wenjun Ding [1], Wei Li [1], Xinhui Fan [1], Yihan Wang [1], Cong Liu [1], Jun Xu [2], Mingjia Bao [2,*], Fenghai Liu [1,*] and Chunjiang Li [1,*]

[1] College of Public Health, Mudanjiang Medical University, Mudanjiang 157011, China; xvjing001024@163.com (J.X.); 15246140878@163.com (W.D.); zgm44317439@163.com (W.L.); fxhxinyi1019@163.com (X.F.); wyihan0061@163.com (Y.W.); 18296477679@163.com (C.L.)
[2] Heilongjiang Provincial Center for Disease Control and Prevention, Harbin 150030, China; hlj6257@163.com
* Correspondence: cmubmj@163.com (M.B.); lfhyxy@126.com (F.L.); lichunjiang@mdjmu.edu.cn (C.L.)

Abstract

An ionic liquid/carboxylated multiwalled carbon nanotube/Cu-ZIF-67 composite was used to modify a glassy carbon electrode (IL/c-MWCNTs@Cu-ZIF-67/GCE) for the individual determination of bisphenol A (BPA) and bisphenol S (BPS). XRD, FTIR, SEM/EDS, and XPS were used to characterize the material, while cyclic voltammetry, electrochemical impedance spectroscopy, and differential pulse voltammetry (DPV) were used to assess electrode behavior and analytical performance. The modified electrode gave higher BPA and BPS oxidation currents than the other electrode configurations. Two linear concentration ranges were obtained for BPA (0.06–1 and 1–100 μM) and BPS (0.1–2 and 2–100 μM), with limits of detection (LODs) of 0.009 and 0.024 μM and estimated limits of quantification (LOQs) of 0.030 and 0.079 μM, respectively. The peak-current RSDs for five independently prepared electrodes were 3.65% for BPA and 3.30% for BPS. After 30 days of storage at 4 °C, 88.4% and 85.6% of the initial responses were retained for BPA and BPS, respectively. Spike-recovery experiments using leachates from polycarbonate drinking cups and polyethersulfone baby bottles gave recoveries of 96.6–101.8%.

Keywords: bisphenols; electrochemical sensor; Cu-ZIF-67; carboxylated multiwalled carbon nanotubes; ionic liquid

1. Introduction

Bisphenol A (BPA) is used in the manufacture of polycarbonate plastics and epoxy resins, which are incorporated into food-contact materials and other consumer products. Its widespread use has raised concerns about human exposure and potential endocrine-related health effects. Recent systematic reviews and meta-analyses have reported associations between BPA exposure and altered male reproductive parameters and metabolic outcomes [1,2]. Bisphenol S (BPS), a structurally related compound, is used as an alternative to BPA in some applications. However, mechanistic evidence indicates that BPS and other BPA analogues may also interact with nuclear receptors and associated signaling pathways [3]. Comparative in vitro studies likewise suggest that replacing BPA with structurally similar compounds does not necessarily remove endocrine-related concerns [4]. Migration from food-contact materials into food and beverages is one potential exposure route. Reviews have documented the migration of bisphenols from food packaging and

Check for updates

Received: 19 October 2026
Revised: 8 November 2026
Accepted: 12 November 2026
Published: 15 November 2026

Copyright: © 2026 by the authors. Licensee MDPI, Basel, Switzerland. This article is an open access article distributed under the terms and conditions of the Creative Commons Attribution (CC BY) license.

discussed how material composition and extraction conditions may influence chemical release [5,6]. These findings motivate analytical methods capable of measuring BPA and its alternatives in relevant sample matrices. Their chemical structures are shown in Figure 1.

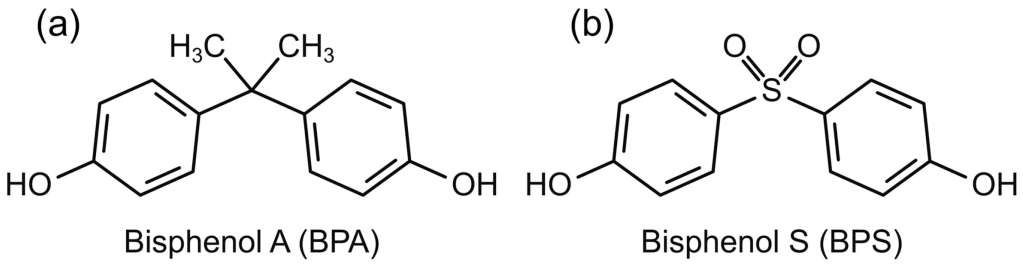
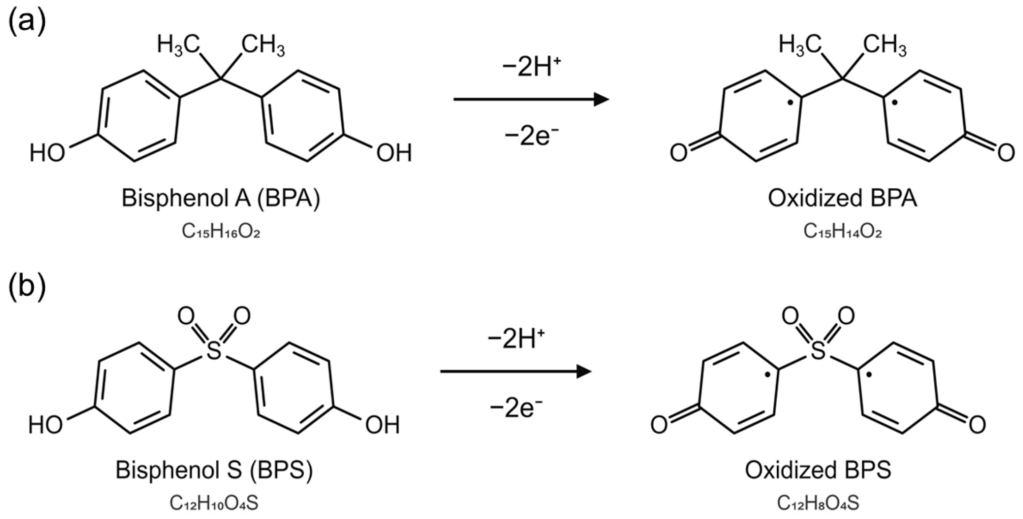


Figure 1. Chemical structures of (**a**) bisphenol A (BPA) and (**b**) bisphenol S (BPS).

Chromatographic techniques, including liquid chromatography coupled with mass spectrometry, are widely used to determine bisphenols in complex samples because they can provide high sensitivity, selectivity, and multi-analyte capability. Özcan et al. described solid-phase extraction combined with LC-PDA-MS/MS for bisphenol derivatives in beverages [7], while Zhan et al. reported a cleanup procedure coupled with ultra-performance liquid chromatography–tandem mass spectrometry for 15 bisphenols in prepared foods [8]. Electrochemical sensing complements chromatographic analysis through simpler instrumentation, opportunities for miniaturization, and rapid voltammetric measurements. The oxidation of BPA and BPS can be monitored voltammetrically, and the response depends on electrode-surface properties, adsorption, and interfacial charge transfer.

Both BPA and BPS contain phenolic hydroxyl groups that serve as electroactive sites for anodic oxidation. Their oxidation involves electron transfer accompanied by proton release, generating the oxidation currents used for their electrochemical determination. Previous studies have proposed the formation of quinonoid oxidation products through an overall two-electron/two-proton pathway for both compounds [9,10], as illustrated in Scheme 1.



Scheme 1. Schematic illustration of the proposed overall two-electron/two-proton anodic oxidation pathways of (**a**) BPA and (**b**) BPS. Oxidized structures are proposed representations and were not independently identified in this study.

Nanomaterial-modified electrodes have been investigated extensively for bisphenol determination. Luis-Sunga et al. used gold nanoparticles and multiwalled carbon nanotubes to modify glassy carbon and screen-printed electrodes for BPA detection [11].

For BPS, Hyder et al. reported a supramolecularly functionalized NiO-based sensor [12], and Mwanza et al. developed a sensing interface based on molecularly imprinted polymers grafted onto functionalized multiwalled carbon nanotubes [13]. The contribution of nanotube conductivity was further highlighted by Liu et al., who found that amino-functionalized MWCNTs enhanced the electrochemical response of a composite electrode toward bisphenols [14]. Other approaches have incorporated covalent organic frameworks or bimetallic metal–organic framework (MOF)/nanotube composites for BPA detection [15,16]. Simultaneous electrochemical determination of BPA and BPS has also been reported using a conductive Fe-based MOF [9], Cu-MOF/Au–Ag composites [17], and a dual-ligand MOF-based electrode for food-contact plastic migration studies [18].

Zeolitic imidazolate framework-67 (ZIF-67), a cobalt-based metal–organic framework composed of cobalt ions and 2-methylimidazolate ligands, provides a porous and compositionally tunable framework for electrode modification. A recent review by Atkare et al. discussed the development of MOF-based composites for bisphenol detection, highlighting the potential of combining MOFs with other functional materials to improve sensing performance [19]. In BPA sensing, combining MIL-100(Fe) with MWCNTs/AuNPs improved the electrode response [20], while incorporating MWCNTs into a ZIF-8-based composite improved its conductivity [21]. The properties of ZIF-67 can be modified by introducing additional metal species. Hu et al. prepared Cu-, Ni-, Fe-, and Zn-modified ZIF-67 for electrochemical glucose sensing [22], while Nakahara and Hitomi investigated Cu-doped ZIF-67 as an artificial laccase catalyst for phenol oxidation [23]. Carbon materials have also been incorporated into ZIF-based composites for electrochemical sensing, including CoCu-ZIF coupled with carbon black [24] and ZIF-67 combined with multiwalled carbon nanotubes [25]. Ionic liquids offer another means of tailoring the interfacial properties of MOF/carbon composites. In a Zr-MOF/graphene-oxide sensing platform, ionic-liquid incorporation was reported to improve dispersibility, conductivity, and adsorption properties for BPA and BPS sensing [26]. Zhang et al. reported a [BMIM][PF_6]-functionalized Zr–Cu bimetallic MOF for nitrite detection [27], and Gorenskaia et al. investigated an ionic liquid/poly(ionic liquid) gel electrolyte to reduce electrode fouling during BPA oxidation [28]. In this study, Cu-ZIF-67 was combined with carboxylated multiwalled carbon nanotubes (c-MWCNTs) and [BMIM][PF_6] to prepare a modified glassy carbon electrode (GCE) for the individual voltammetric determination of BPA and BPS. BPS was included to assess whether the platform initially developed for BPA could also be applied to a structurally related alternative. The electrochemical responses of different electrode configurations were compared, and the analytical performance of the resulting sensor was evaluated in terms of calibration characteristics, selectivity, reproducibility, storage stability, and spike recoveries in plastic leachates.

2. Materials and Methods

2.1. Chemicals and Reagents

Cobalt(II) nitrate hexahydrate ($Co(NO_3)_2{\cdot}6H_2O$), copper(II) nitrate trihydrate ($Cu(NO_3)_2{\cdot}3H_2O$), 2-methylimidazole, methanol, bisphenol A (BPA), bisphenol S (BPS), 1-butyl-3-methylimidazolium hexafluorophosphate ([BMIM][PF_6]; 97% purity), concentrated sulfuric acid (H_2SO_4), concentrated nitric acid (HNO_3), N,N-dimethylformamide (DMF), sodium dihydrogen phosphate (NaH_2PO_4), disodium hydrogen phosphate (Na_2HPO_4), potassium ferricyanide ($K_3[Fe(CN)_6]$), potassium ferrocyanide trihydrate ($K_4[Fe(CN)_6]{\cdot}3H_2O$), potassium chloride (KCl), phenol, catechol, resorcinol, and hydroquinone were purchased from Aladdin (Shanghai, China). Pristine multiwalled carbon nanotubes (MWCNTs; length, 10–30 μm; outer diameter, 5–15 nm) were purchased from

XFNANO (Nanjing, China). Carboxylated MWCNTs (c-MWCNTs) were prepared by acid oxidation as described in Section 2.3.1.

Phosphate buffer was selected as the supporting electrolyte based on its established use in previous electrochemical studies of BPA and BPS [11,18]. A 0.2 M phosphate-buffered solution (PBS) was prepared by mixing 0.2 M NaH_2PO_4 and 0.2 M Na_2HPO_4 solutions in appropriate proportions to obtain the required pH. Unless otherwise stated, electrochemical measurements were performed in PBS at pH 7.0. Buffer solutions were prepared fresh before use.

Potassium ferricyanide ($K_3[Fe(CN)_6]$), potassium ferrocyanide trihydrate ($K_4[Fe(CN)_6]\cdot 3H_2O$), and potassium chloride (KCl) were used to prepare the redox probe solution. The probe solution was prepared by dissolving 0.1645 g of $K_3[Fe(CN)_6]$ and 0.2112 g of $K_4[Fe(CN)_6]\cdot 3H_2O$ in 0.1 M KCl solution and bringing the final volume to 100 mL. It contained 5.0 mM of each redox component and 0.1 M KCl and was stored at 4 °C in the dark. Unless otherwise specified, chemical reagents were of analytical grade and used without further purification. Ultrapure water with a resistivity of 18.2 MΩ·cm was used throughout the experiments.

Commercial polycarbonate (PC) drinking cups and polyethersulfone (PES) baby bottles were purchased from a local supermarket for the plastic-leachate experiments.

2.2. Instrumentation

All electrochemical measurements were performed using a PGSTAT302N electrochemical workstation (Metrohm Autolab, Utrecht, the Netherlands) controlled by NOVA software (version 2.1.4), with a conventional three-electrode system consisting of a glassy carbon electrode (GCE, 3 mm in diameter; Tianjin Aida Hengsheng S&T Development Co., Ltd., Tianjin, China) as the working electrode, an Ag/AgCl electrode (saturated KCl; Shanghai Chenhua Instrument Co., Ltd., Shanghai, China) as the reference electrode, and a platinum wire (0.5 mm in diameter; Tianjin Aida Hengsheng Technology Development Co., Ltd., Tianjin, China) as the counter electrode.

The pH of the buffer solutions was measured and adjusted using a pHS-25 pH meter (Shanghai Jingke, Shanghai, China). Ultrasonic treatment was performed using a KQ2200DV ultrasonic cleaner (Kunshan Ultrasonic Instruments Co., Ltd., Kunshan, China), while magnetic stirring and heating were carried out using a C-MAG HS 10 magnetic hotplate stirrer (IKA, Staufen, Germany). The synthesized materials were collected using an H2500R-2 centrifuge (Hunan Xiangyi, Changsha, China). Reagents were weighed using an analytical balance (Model 204, Mettler Toledo, Greifensee, Switzerland). Plastic leaching experiments were conducted using an HWS-24 thermostatic water bath (Shanghai Yiheng Scientific Instrument Co., Ltd., Shanghai, China).

The surface morphology was examined by field-emission scanning electron microscopy (FE-SEM; MIRA 3 GMU, TESCAN, Brno, Czech Republic) at 15 kV, and elemental composition was analyzed by energy-dispersive X-ray spectroscopy (EDS). Samples were sputter-coated with gold before examination. X-ray diffraction (XRD) patterns were recorded using a D8 Advance diffractometer (Bruker, Karlsruhe, Germany). Fourier-transform infrared (FTIR) spectra were recorded using a Nicolet iS20 FTIR spectrometer (Thermo Scientific, Madison, WI, USA) to examine functional groups, and X-ray photoelectron spectroscopy (XPS) was performed using a Thermo Scientific 250Xi instrument (Thermo Fisher Scientific, East Grinstead, UK) to examine surface chemical states.

Ultrapure water with a resistivity of 18.2 MΩ·cm was produced using a PureLab Classic ultrapure water purification system (ELGA, High Wycombe, UK).

Background screening of the undiluted plastic leachates and quantitative analysis of the spiked leachate samples were carried out using an UltiMate 3000 liquid chromatography system (Thermo Scientific Dionex, Germering, Germany).

2.3. Preparation of c-MWCNTs and Cu-ZIF-67-Based Materials

2.3.1. Preparation of Carboxylated Multi-Walled Carbon Nanotubes

Carboxylated MWCNTs (c-MWCNTs) were obtained by acid oxidation of pristine MWCNTs. Briefly, 200 mg of MWCNTs was added to 20 mL of concentrated H_2SO_4/HNO_3 (3:1, *v*/*v*) and refluxed at 80 °C with magnetic stirring at 500 rpm for 6 h. After cooling, the mixture was diluted with deionized water and centrifuged at 10,000 rpm. The collected solid was washed repeatedly with ultrapure water until the supernatant reached neutral pH, and then vacuum freeze-dried to obtain c-MWCNTs.

2.3.2. Synthesis of ZIF-67

Pristine ZIF-67 was synthesized without copper salts or carbon nanotubes. Briefly, 2.626 g (32 mmol) of 2-methylimidazole (2-MIM) was dissolved in 40 mL of anhydrous methanol and stirred at room temperature for 30 min. Separately, 1.164 g (4.0 mmol) of $Co(NO_3)_2{\cdot}6H_2O$ was dissolved in a small amount of methanol and rapidly added to the ligand solution. The Co^{2+}-to-2-MIM molar ratio was 1:8. The reaction mixture was stirred at room temperature for 1 h and then left undisturbed for 24 h. The precipitate was recovered by centrifugation, washed several times with methanol, and vacuum-dried at 60 °C to obtain ZIF-67.

2.3.3. Synthesis of Cu-ZIF-67

Cu-ZIF-67 was prepared using the same metal-to-ligand ratio and the same reaction, aging, washing, and drying conditions as those employed for the c-MWCNTs@Cu-ZIF-67 composite (Section 2.3.4), except that c-MWCNTs were not added. Specifically, 2.626 g (32 mmol) of 2-MIM was mixed with 40 mL of anhydrous methanol and stirred for 30 min. A methanolic solution containing 0.931 g (3.2 mmol) of $Co(NO_3)_2{\cdot}6H_2O$ and 0.193 g (0.8 mmol) of $Cu(NO_3)_2{\cdot}3H_2O$ was then rapidly added. After stirring at room temperature for 1 h and aging without stirring for 24 h, the product was separated by centrifugation, washed repeatedly with methanol, and vacuum-dried at 60 °C. No carbon nanotubes were used in this preparation.

2.3.4. Synthesis of c-MWCNTs@Cu-ZIF-67 Composites

To synthesize the c-MWCNTs@Cu-ZIF-67 composite, 40 mg of c-MWCNTs was dispersed in 40 mL of anhydrous methanol by ultrasonication for 30 min to obtain a homogeneous suspension. Subsequently, 2.626 g (32 mmol) of 2-methylimidazole was added under magnetic stirring, and stirring was continued for another 30 min.

Separately, 0.931 g (3.2 mmol) of $Co(NO_3)_2{\cdot}6H_2O$ and 0.193 g (0.8 mmol) of $Cu(NO_3)_2{\cdot}3H_2O$ were dissolved in a small amount of methanol. The resulting metal precursor solution was rapidly poured into the above suspension. The mixture was stirred at room temperature for 1 h and then allowed to age without stirring for 24 h.

The resulting precipitate was collected by centrifugation, washed several times with methanol, and dried under vacuum at 60 °C to obtain the c-MWCNTs@Cu-ZIF-67 composite.

2.4. Pretreatment and Modification of the Glassy Carbon Electrode

Before modification, the bare glassy carbon electrode (GCE) was polished with 0.3 μm and 0.05 μm alumina slurries in sequence on a polishing cloth to give a mirror-like surface. The electrode was then ultrasonically cleaned in nitric acid, anhydrous ethanol, and pure

water, respectively, to remove residual particles. The cleaned GCE was then electrochemically activated by cyclic voltammetry in 0.5 M H_2SO_4 over a potential range of −0.5 to +1.5 V (vs. Ag/AgCl, saturated KCl) at 50 mV s^{-1} for 20 cycles. Finally, the electrode was rinsed again with ultrapure water and allowed to air-dry at room temperature before use.

To prepare the electrode-modifying suspension, 20.0 mg of the as-synthesized c-MWCNTs@Cu-ZIF-67 composite and 25 µL of [BMIM][PF_6] were dispersed in 10 mL of DMF by ultrasonication for 30 min. Subsequently, 5 µL of the homogeneous suspension was drop-cast onto the surface of a pretreated GCE and allowed to dry at room temperature. The resulting modified electrode was denoted as IL/c-MWCNTs@Cu-ZIF-67/GCE.

2.5. Electrochemical Measurements and Data Analysis

BPA and BPS were determined separately by differential pulse voltammetry (DPV). For each measurement, the IL/c-MWCNTs@Cu-ZIF-67/GCE was immersed in 0.2 M PBS (pH 7.0) containing the respective analyte. Before each DPV scan, the analyte was accumulated at an applied potential of 0.2 V for 300 s. DPV scans were recorded over 0.2–0.8 V for BPA and 0.4–1.0 V for BPS. The potential increment, pulse amplitude, and pulse width were 0.005 V, 0.05 V, and 0.05 s, respectively, for both analytes. CV and EIS responses of the control and composite-modified electrodes were measured in a redox-probe solution containing 5.0 mM $K_3[Fe(CN)_6]$, 5.0 mM $K_4[Fe(CN)_6]\cdot 3H_2O$, and 0.1 M KCl. Comparative CV measurements were performed from −0.2 to +0.6 V (vs. Ag/AgCl) at 50 mV s^{-1} for three cycles. EIS was recorded at the open-circuit potential (OCP) from 100 kHz to 1 Hz with a 10 mV (RMS) sinusoidal perturbation.

BPA and BPS were identified by their individual oxidation peak positions and quantified from their corresponding oxidation peak currents. Calibration relationships were obtained by unweighted least-squares linear regression. All electrochemical measurements were carried out at room temperature, and all reported potentials refer to the Ag/AgCl (saturated KCl) reference electrode.

2.6. Preparation of Plastic Leachates and Spike-Recovery Tests

Commercial PC drinking cups and PES baby bottles were used to prepare leachate matrices for BPA and BPS analyses, respectively. Each material was cut into small pieces, and 2.0 g was immersed in 20 mL of ultrapure water at 70 °C for 24 h. The containers were sealed and maintained in a thermostatic water bath during the 24 h leaching period. After cooling to room temperature, the leachates were filtered through 0.22 µm membranes. The filtrates were stored at 4 °C in the dark and analyzed within 24 h. Aliquots of the original, undiluted leachates were screened for BPA and BPS by liquid chromatography before the electrochemical experiments. Separate aliquots were diluted fivefold with 0.2 M PBS (pH 7.0) for subsequent spike-recovery measurements. BPA standards were added to the diluted PC leachate at final concentrations of 0.1, 1.0, and 10.0 µM; BPS standards were added to the diluted PES leachate at 0.5, 5.0, and 20.0 µM. Each spiked solution was measured in triplicate ($n = 3$). The spiked leachates were also analyzed by HPLC to compare the results with those obtained using the proposed electrochemical method. Spike recovery was calculated from the mean concentration back-calculated from the three peak currents. The relative standard deviation (RSD) was calculated from the three corresponding back-calculated concentrations at each spike level. This protocol provided accelerated aqueous leachate matrices for assessing the analytical method.

3. Results and Discussion

3.1. Structural and Morphological Characterization

3.1.1. X-Ray Diffraction

The XRD pattern of ZIF-67 showed reflections at 7.38°, 10.42°, 12.76°, 14.70°, 16.40°, and 18.08° (Figure 2a), consistent with the characteristic ZIF-67 structure. Cu-ZIF-67 retained the principal ZIF-67 reflections, and no additional crystalline phases were resolved. The first reflection shifted slightly from 7.38° to 7.28° after the Cu-containing synthesis. The principal ZIF-67 reflections were also present in c-MWCNTs@Cu-ZIF-67, indicating that the crystalline framework was largely retained in the composite.

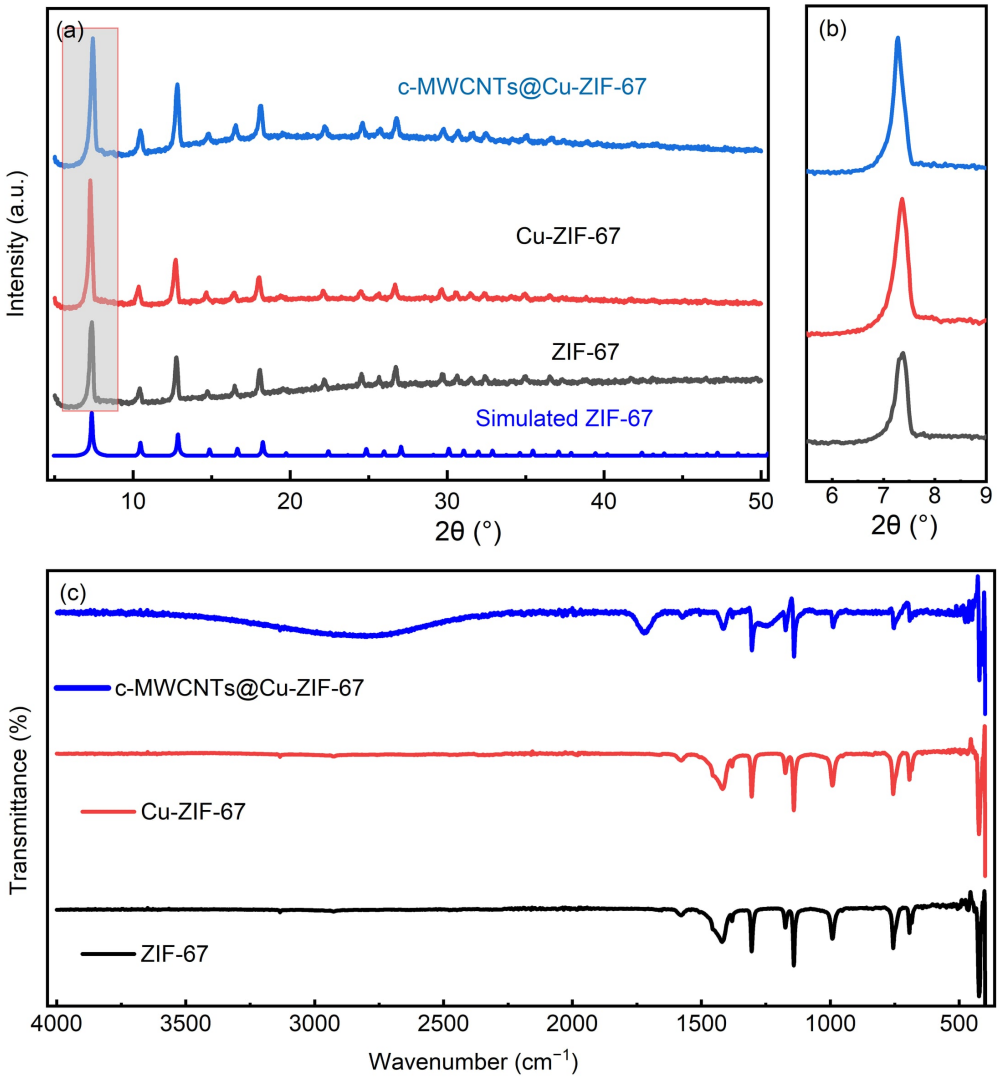


Figure 2. Structural characterization of ZIF-67, Cu-ZIF-67, and c-MWCNTs@Cu-ZIF-67: (**a**) XRD patterns, including the simulated ZIF-67 reference pattern; (**b**) enlarged view of the gray-shaded low-angle XRD region in (**a**); and (**c**) FTIR spectra. The curves are color-coded and identified by the labels in (**a**) and (**c**).

3.1.2. Fourier Transform Infrared Spectroscopy

The FTIR spectrum of ZIF-67 (Figure 2c) showed bands at 1586, 1422, 1304, 1174, 1141, 989, 756, 694, and 426 cm^{-1}, associated with the imidazolate ligand and Co–N coordination. The main ZIF-67 bands remained in Cu-ZIF-67, although the bands at 1586 and 426 cm^{-1} shifted to 1575 and 423 cm^{-1}, respectively. These shifts suggest changes in the local coordi-

nation environment. The composite retained the characteristic ZIF-67 bands. A feature near 1722 cm^{-1} was assigned to carbonyl stretching of carboxyl-containing groups, while the broad band at approximately 2322–3464 cm^{-1} was associated mainly with O–H-containing species and adsorbed water.

3.1.3. Scanning Electron Microscopy and EDS

Pristine ZIF-67 formed faceted polyhedral particles with well-defined edges and relatively smooth surfaces (Figure 3a). Cu-ZIF-67 displayed a similar polyhedral morphology (Figure 3b), showing that the overall particle shape was retained after the Cu-containing synthesis. The c-MWCNTs@Cu-ZIF-67 composite retained a recognizable polyhedral morphology, with numerous entangled nanotubes distributed over the particle surfaces (Figure 3c). Some nanotubes extended between adjacent particles, forming interparticle connections. The EDS spectrum (Figure 3d) showed C, N, O, Co, and Cu signals, consistent with the elemental composition of the composite.

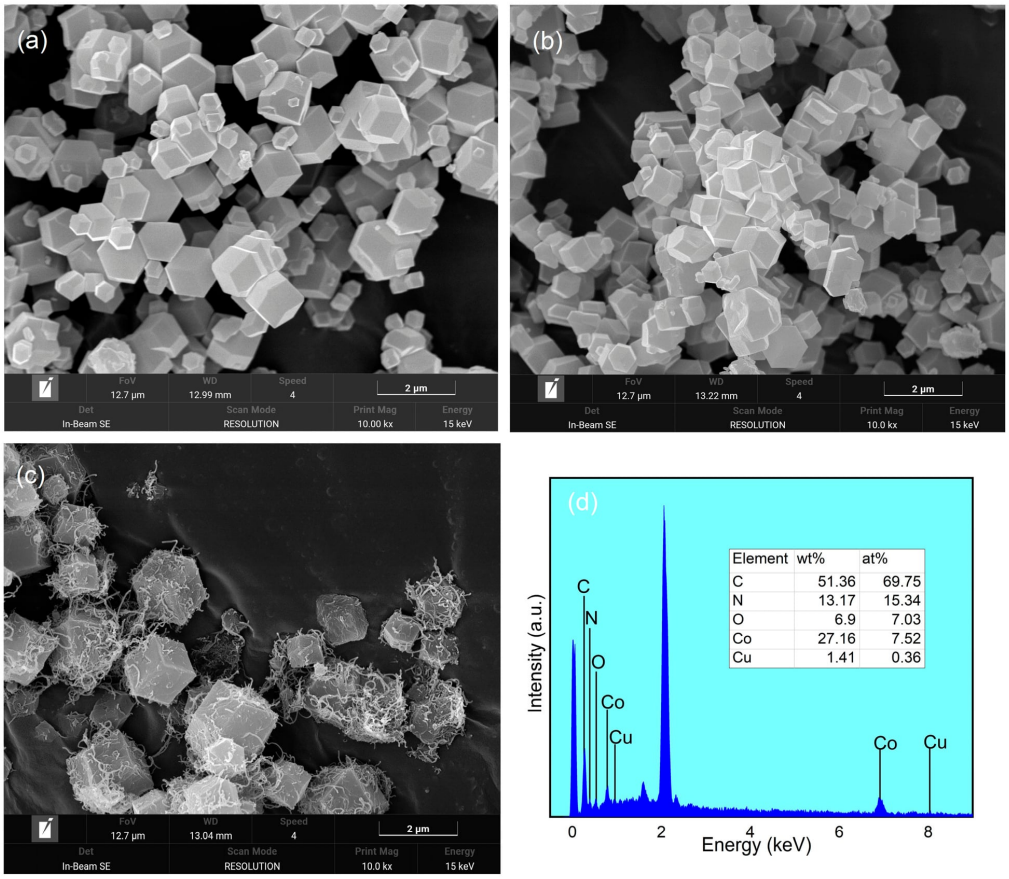


Figure 3. Morphology and elemental characterization: representative SEM images of (**a**) ZIF-67, (**b**) Cu-ZIF-67, and (**c**) c-MWCNTs@Cu-ZIF-67, and (**d**) EDS spectrum of the c-MWCNTs@Cu-ZIF-67 composite.

3.1.4. X-Ray Photoelectron Spectroscopy

The XPS survey spectrum of c-MWCNTs@Cu-ZIF-67 showed signals from C, N, O, Co, and Cu (Figure 4a). High-resolution spectra were then examined to assess the surface bonding environments. The high-resolution C 1s spectrum (Figure 4b) was fitted with components at 284.78, 285.83, 287.23, 288.88, and 290.88 eV, assigned to C–C/C=C, C–O, C=O, carboxyl-related carbon, and a π–π^* satellite feature, respectively. The assignments are consistent with carbon-containing framework and nanotube surface groups. The N

1s spectrum (Figure 4c) showed fitted components at 398.93 and 400.58 eV, assigned to coordination-associated nitrogen and C–N environments, respectively. The O 1s components at 531.78 and 534.02 eV were attributed to oxygen-containing surface groups (Figure 4d). The Co 2p spectrum (Figure 4e) contained major features at 781.21 and 797.08 eV, assigned to Co $2p_3/_2$ and Co $2p_1/_2$, together with satellite features at 786.63 and 802.98 eV. The observed pattern is consistent with Co(II)-containing surface species. The Cu 2p spectrum (Figure 4f) displayed components at 933.41 and 954.44 eV, assigned to Cu $2p_3/_2$ and Cu $2p_1/_2$, and satellite features at 942.54 and 961.18 eV. The satellite structure is consistent with Cu(II)-containing surface species.

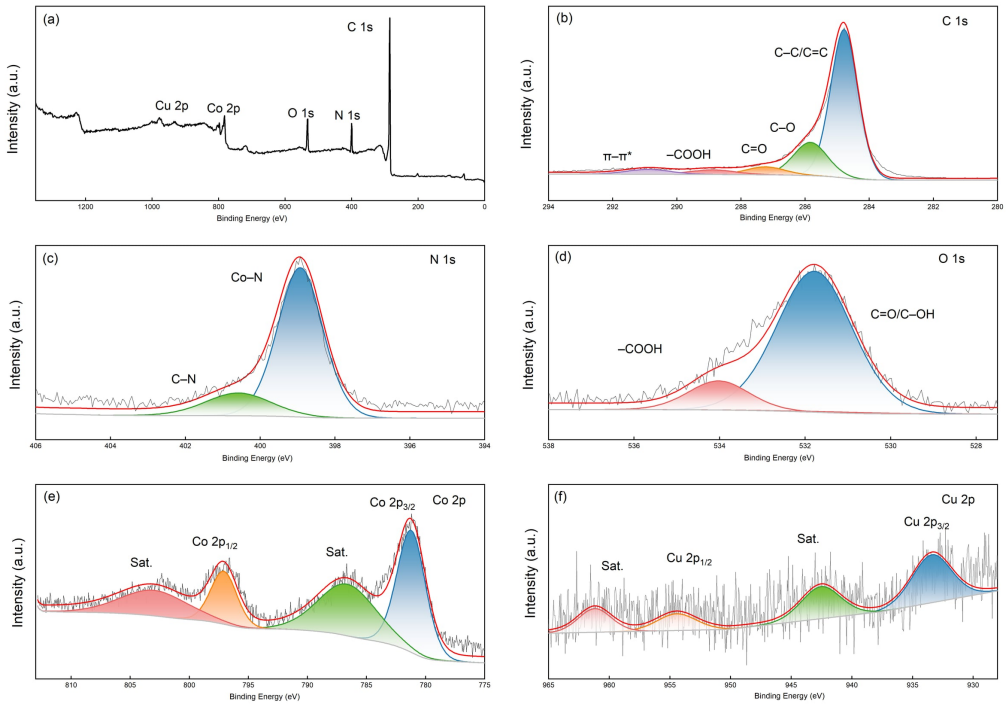


Figure 4. XPS characterization of c-MWCNTs@Cu-ZIF-67: (**a**) survey spectrum and high-resolution spectra of (**b**) C 1s, (**c**) N 1s, (**d**) O 1s, (**e**) Co 2p, and (**f**) Cu 2p. In (b–f), the gray traces represent the experimental spectra, the red curves indicate the overall fits, and the colored shaded peaks correspond to the deconvoluted components.

Together, the XRD and FTIR results indicate that the main ZIF-67 framework was retained after Cu introduction, while the observed peak shifts suggest changes in the local structural environment. The XPS results further confirm the presence of Co(II)- and Cu(II)-containing species in the composite.

3.2. Electrochemical Characterization of Modified Electrodes

3.2.1. Cyclic Voltammetry

CV measurements in the ferri/ferrocyanide probe solution revealed differences among the bare and modified electrodes (Figure 5a). Compared with bare GCE, ZIF-67/GCE showed lower peak currents and a larger peak separation. The probe current increased after Cu incorporation and increased further with the addition of c-MWCNTs. The IL-containing composite maintained a higher current than bare GCE, although its probe current was slightly lower than that of the corresponding IL-free composite.

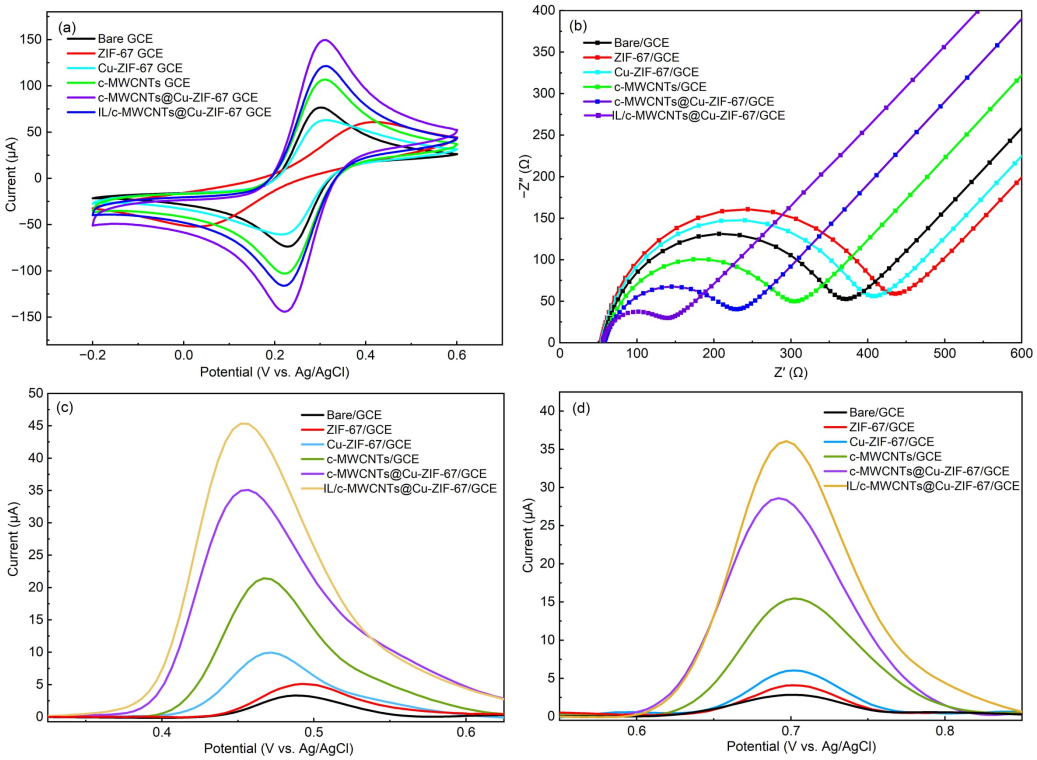


Figure 5. Electrochemical responses of bare and modified glassy carbon electrodes: (**a**) cyclic voltammograms and (**b**) EIS Nyquist plots in the ferri/ferrocyanide redox-probe solution; DPV responses to individually measured 50 μM (**c**) BPA and (**d**) BPS in 0.2 M phosphate buffer (pH 7.0). The respective tests were conducted under their specified electrochemical conditions.

3.2.2. Electrochemical Impedance Spectroscopy

The Nyquist plots showed a trend consistent with the CV results (Figure 5b). ZIF-67/GCE exhibited a larger semicircle than bare GCE, indicating higher interfacial charge-transfer resistance. The semicircle diameter decreased after Cu introduction and further incorporation of c-MWCNTs, consistent with the increased redox-probe peak currents observed in the CV measurements (Figure 5a). These results indicate improved interfacial charge-transfer behavior at Cu-ZIF-67/GCE compared with ZIF-67/GCE. The addition of [BMIM][PF_6] resulted in a slight increase in the semicircle diameter relative to the IL-free composite.

3.2.3. DPV Responses of BPA and BPS at Different Modified Electrodes

DPV responses were compared at six electrode configurations using 50 μM BPA and 50 μM BPS in separate measurements (Figure 5c,d). Bare GCE gave the weakest oxidation response for both analytes. ZIF-67/GCE and Cu-ZIF-67/GCE produced larger signals, and the c-MWCNT-modified electrodes showed further increases.

Among the electrodes examined, IL/c-MWCNTs@Cu-ZIF-67/GCE exhibited the highest oxidation peak currents for both BPA and BPS (Figure 5c,d). The incorporation of [BMIM][PF_6] further enhanced the analytical responses, despite a slight decrease in the ferri/ferrocyanide peak current and an increase in the EIS semicircle diameter relative to the IL-free composite (Figure 5a,b). These results demonstrate the beneficial effect of the ionic liquid on the electrochemical detection of both bisphenols. The enhanced responses are consistent with the adsorption-related behavior of BPA and BPS and the favorable interfacial environment provided by the IL-containing composite.

3.2.4. Electrochemically Active Surface Area

The electrochemically active surface area (ECSA) was estimated according to the Randles–Sevcik equation:

$$I_p = 2.69 \times 10^5 \, n^{3/2} \, A \, D^{1/2} \, C \, v^{1/2}$$

In the Randles–Sevcik equation, I_p is the anodic peak current (A); n is the electron-transfer number of the $[Fe(CN)_6]^{3-/4-}$ probe ($n = 1$); D is the adopted literature diffusion coefficient for the ferri/ferrocyanide couple (6.70×10^{-6} cm^2 s^{-1}) [29]; C is the redox-probe concentration (5.0×10^{-6} mol cm^{-3}); and v is the scan rate (V s^{-1}). The slopes obtained from Figure 6c were converted from the plotted peak-current and scan-rate units to these equation units. The calculated electrochemically active surface areas were 0.080 cm^2 for the bare GCE and 0.260 cm^2 for IL/c-MWCNTs@Cu-ZIF-67/GCE, corresponding to a 3.25-fold increase.

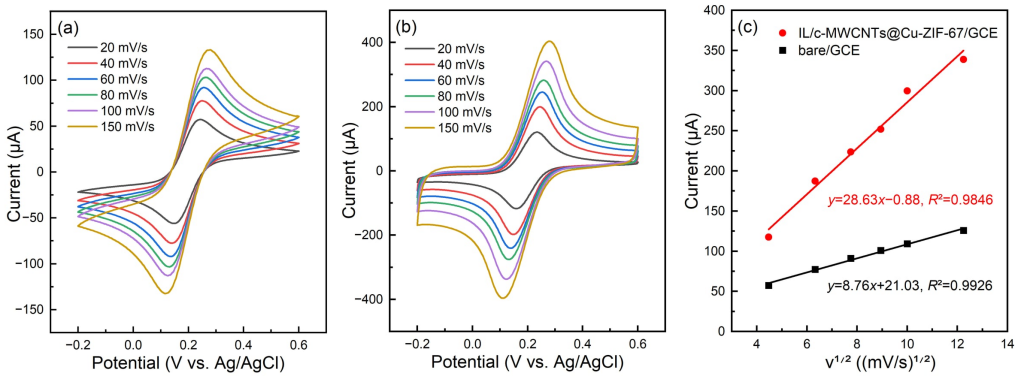


Figure 6. Electrochemically active surface area characterization: CVs of (**a**) bare GCE and (**b**) IL/c-MWCNTs@Cu-ZIF-67/GCE recorded at 20, 40, 60, 80, 100, and 150 mV s^{-1} between −0.2 and +0.6 V in ferri/ferrocyanide solution; (**c**) anodic peak-current relationships with the square root of scan rate. The area estimates were obtained using the Randles–Sevcik equation.

3.3. Effect of Scan Rate

CV measurements were carried out at 20–200 mV s^{-1} to examine the oxidation behavior of 50 μM BPA and BPS separately (Figure 7a,b). The potential ranges were −0.1 to +0.7 V for BPA and −0.1 to +1.0 V for BPS. In both cases, the oxidation current increased and the peak potential shifted positively as the scan rate increased.

For BPA, the baseline-corrected oxidation peak current increased linearly with scan rate: $I_{pa} = 0.0382v + 1.787$ ($R^2 = 0.997$; Figure 7c). The corresponding fit against the square root of scan rate gave $R^2 = 0.983$.

BPS showed a similar dependence, with $I_{pa} = 0.0255v + 0.890$ ($R^2 = 0.988$), compared with $R^2 = 0.978$ for the square-root relationship. Here, I_{pa} is expressed in μA and v in mV s^{-1}. The stronger I_{pa}–v correlations suggest a substantial adsorption-controlled contribution for both analytes.

The oxidation peak potentials were also linear with $\ln[v/(\text{V s}^{-1})]$ (Figure 7d): $E_{pa} = 0.0109 \ln[v/(\text{V s}^{-1})] + 0.539$ ($R^2 = 0.978$) for BPA and $E_{pa} = 0.0178 \ln[v/(\text{V s}^{-1})] + 0.798$ ($R^2 = 0.965$) for BPS. The positive potential shifts are consistent with kinetically irreversible oxidation.

These scan-rate results indicate an adsorption-related contribution to peak-current generation and kinetically irreversible oxidation for both analytes.

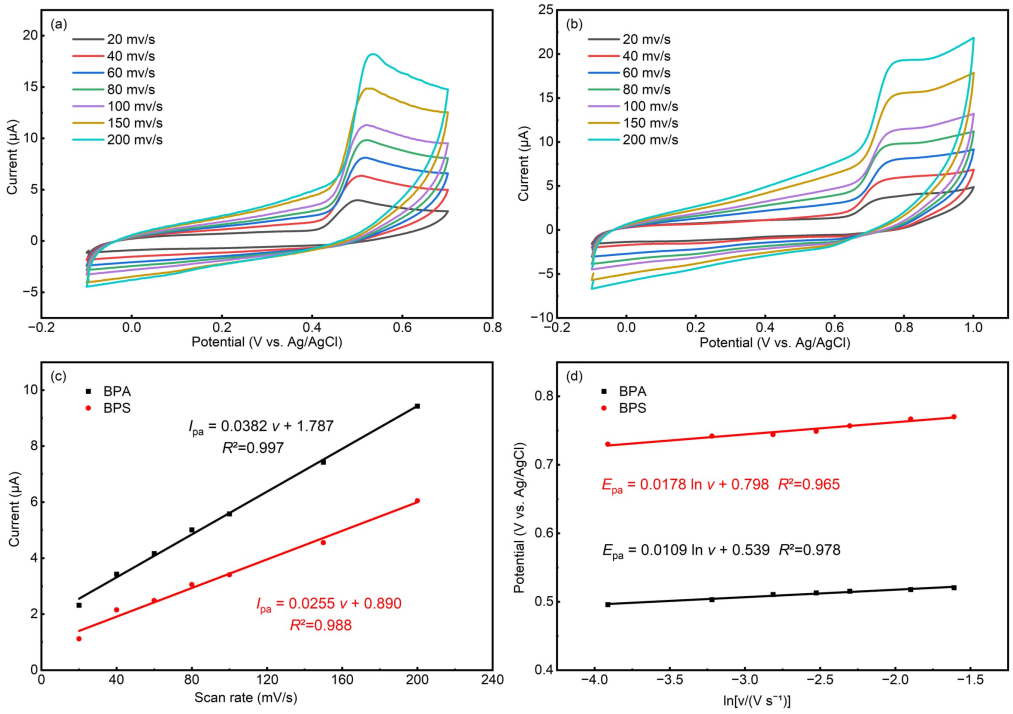


Figure 7. Effect of scan rate on the individual electrochemical oxidation of BPA and BPS at IL/c-MWCNTs@Cu-ZIF-67/GCE: CVs of (**a**) BPA (−0.1 to +0.7 V) and (**b**) BPS (−0.1 to +1.0 V) at 20–200 mV s^{-1}; (**c**) baseline-corrected anodic peak currents plotted against scan rate; and (**d**) oxidation peak potentials plotted against $\ln[v/(\mathrm{V\ s^{-1}})]$.

3.4. Optimization of Experimental Conditions

3.4.1. Effect of Solution pH

The effect of pH was examined for 50 μM BPA and BPS in separate DPV measurements using 0.2 M phosphate buffer (pH 6.0–8.0; Figure 8). Both peak currents reached a maximum at pH 7.0, which was selected for subsequent measurements.

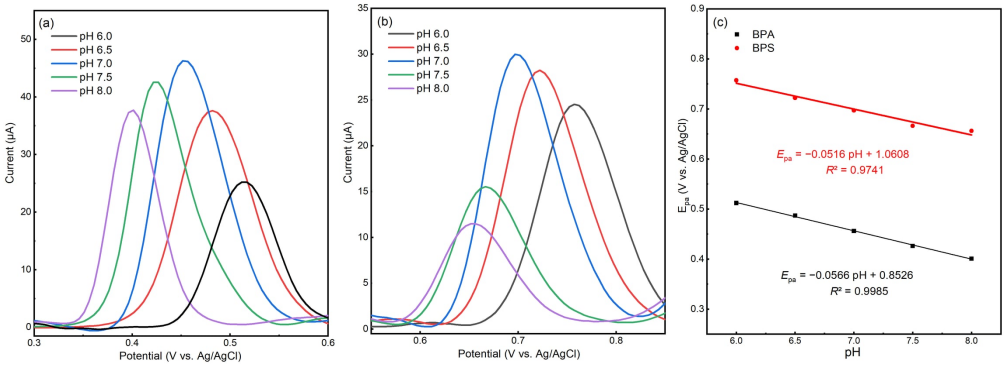


Figure 8. Effect of phosphate buffer pH (6.0–8.0) on the individual DPV oxidation responses of 50 μM (**a**) BPA and (**b**) BPS at IL/c-MWCNTs@Cu-ZIF-67/GCE, and (**c**) the relationships between anodic peak potential and pH. The buffer concentration was 0.2 M.

The oxidation peak potentials of both analytes shifted negatively with increasing pH (Figure 8c). Linear regression yielded E_{pa} = −0.0566 pH + 0.8526 (R^2 = 0.9985) for BPA and E_{pa} = −0.0516 pH + 1.0608 (R^2 = 0.9741) for BPS, corresponding to −56.6 and −51.6 mV per pH unit, respectively. These systematic shifts support proton involvement in the electrochemical oxidation processes.

Above pH 7.0, the BPS current decreased more strongly than the BPA current, indicating different pH dependences for the two oxidation responses.

3.4.2. Optimization of Electrode Preparation and Accumulation Conditions

Composite concentration, ionic-liquid volume, drop-casting volume, and accumulation time were optimized separately using 50 μM BPA and BPS in separate measurements (Figure 9a–d).

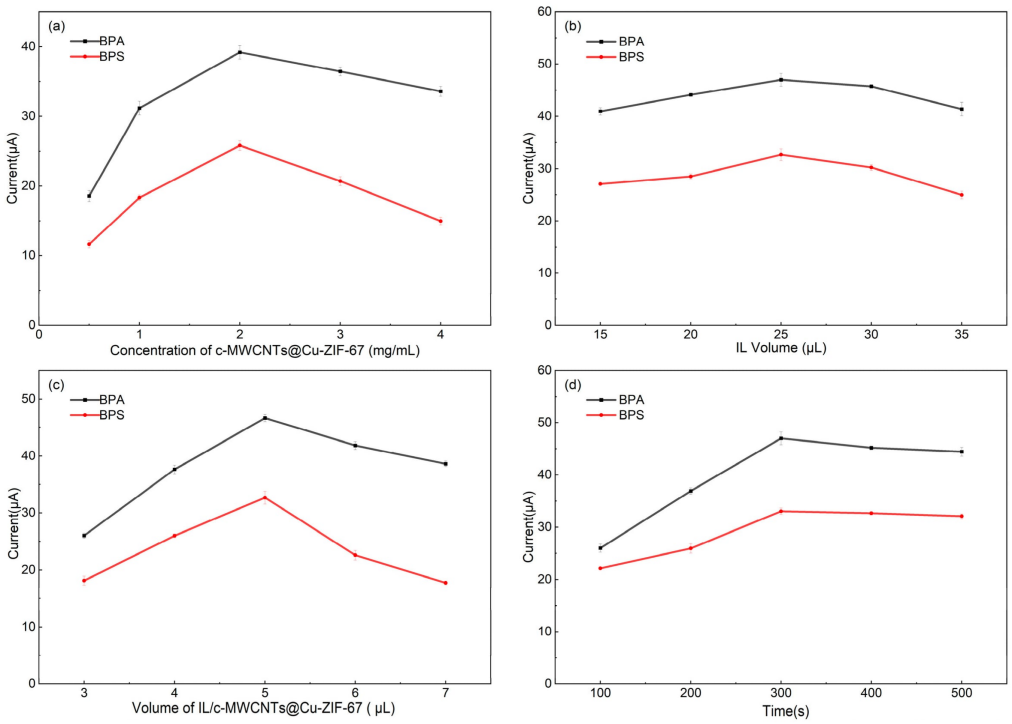


Figure 9. Optimization of electrode preparation and measurement conditions for the individual determination of BPA and BPS: effects of (**a**) composite dispersion concentration, (**b**) volume of [BMIM][PF_6] in the dispersion, (**c**) drop-casting volume, and (**d**) accumulation time on the anodic peak current.

The largest oxidation currents were obtained at a composite concentration of 2.0 mg mL^{-1} (Figure 9a). Higher concentrations gave smaller responses, and 2.0 mg mL^{-1} was selected for electrode preparation.

At the optimized composite concentration of 2.0 mg mL^{-1}, the peak currents increased as the [BMIM][PF_6] volume was raised to 25 μL and decreased at higher volumes (Figure 9b). An ionic-liquid volume of 25 μL was therefore used.

A 5 μL drop-casting volume of the resulting suspension (2.0 mg mL^{-1} composite) gave the maximum response for both analytes (Figure 9c) and was used in subsequent experiments.

The peak currents increased between 100 and 300 s of accumulation and changed little with further accumulation up to 500 s (Figure 9d). An accumulation time of 300 s was chosen.

3.5. Calibration Characteristics

Separate DPV calibration curves were obtained under the optimized conditions. For BPA (Figure 10a,c), the unweighted linear fits were $I_{pa} = 10.210C + 0.817$ ($R^2 = 0.9981$) over

0.06–1 μM and I_{pa} = 0.755*C* + 9.909 (R^2 = 0.9983) over 1–100 μM, where I_{pa} is the anodic peak current in μA and *C* is the concentration in μM.

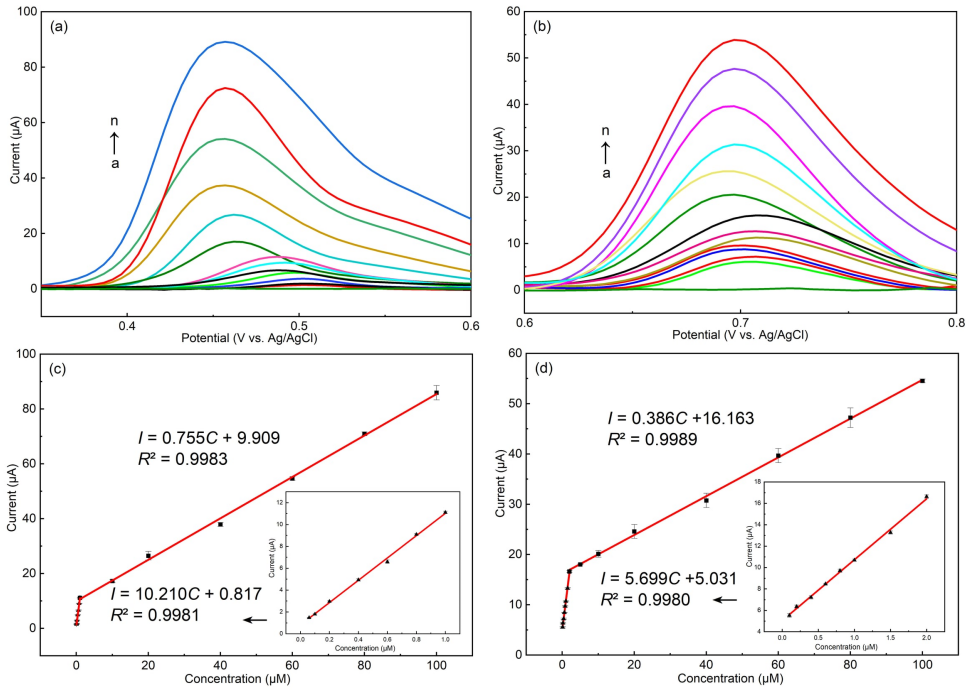


Figure 10. Individual DPV determination of BPA and BPS at IL/c-MWCNTs@Cu-ZIF-67/GCE: concentration-dependent DPV responses of (**a**) BPA (0.06–100 μM) and (**b**) BPS (0.1–100 μM). Curves a–n in (**a**) correspond to blank, 0.06, 0.1, 0.2, 0.4, 0.6, 0.8, 1, 10, 20, 40, 60, 80, and 100 μM BPA, respectively; curves a–n in (**b**) correspond to blank, 0.1, 0.2, 0.4, 0.6, 0.8, 1, 2, 10, 20, 40, 60, 80, and 100 μM BPS, respectively. The arrows in (**a**,**b**) indicate increasing analyte concentrations. The corresponding segmented calibration relationships are shown in (**c**,**d**). Insets show the low-concentration calibration segments. Error bars in (**c**,**d**) represent the standard deviation of three replicate measurements (n = 3).

For BPS (Figure 10b,d), the corresponding relationships were I_{pa} = 5.699*C* + 5.031 (R^2 = 0.9980) over 0.1–2 μM and I_{pa} = 0.386*C* + 16.163 (R^2 = 0.9989) over 2–100 μM.

The limits of detection (LODs) and estimated limits of quantification (LOQs) were calculated using LOD = 3σ/m and LOQ = 10σ/m, respectively, where σ is the standard deviation of 20 blank measurements and m is the slope of the low-concentration calibration segment. The LODs were 0.009 μM for BPA and 0.024 μM for BPS, while the corresponding estimated LOQs were 0.030 and 0.079 μM, respectively.

As shown in Figure 10a, the oxidation peak potential of BPA exhibited an overall shift toward less positive potentials as the concentration increased, changing from approximately 0.502 V at lower concentrations to 0.456 V at higher concentrations. In contrast, the oxidation peak potential of BPS remained relatively stable within 0.697–0.707 V (Figure 10b). A concentration-dependent negative shift in the BPA oxidation peak potential has also been reported by Chen et al. in DPV measurements using a photoelectrochemical sensing platform [30]. Considering the adsorption-related behavior indicated by the scan-rate experiments (Figure 7), the observed shift may be associated with changes in analyte adsorption and interfacial oxidation behavior at different concentrations. However, the specific contribution of these factors cannot be determined from the present results.

The analytical figures of merit were compared with selected individually and simultaneously operating BPA and BPS electrochemical sensors (Table 1). In this comparison, the proposed sensor achieved LODs of 0.009 μM for BPA and 0.024 μM for BPS, respectively,

which are lower than those reported for most of the corresponding electrochemical platforms. Differences in sensing architecture, assay mode, and validation matrices should be considered when interpreting the values.

Table 1. Comparison of selected electrochemical platforms for BPA and/or BPS determination. Linear ranges and limits of detection (LODs) are taken from the cited reports, with individual and simultaneous assays distinguished.

Electrode/Platform	Analyte	Mode	Linear Range (μM)	LOD (μM)	Ref.
Cu, Ni-BTC/CNT	BPA	Individual	2–50	0.500	[16]
B14C4-Py-COF/MWCNT/GCE	BPA	Individual	0.5–600	0.130	[15]
Pt@COOH-MWCNT/PVA/AM hydrogel/GCE	BPA	Individual	0.05–1000	0.045	[31]
$CuWO_4$/f-MWCNT/GCE	BPA	Individual	0.05–160	0.040	[32]
WS_2/Fe_3O_4/rGO/LabSPE	BPA	Individual	0.05–50	0.030	[33]
CTpPa-2/GCE	BPA	Simultaneous	0.1–2.5; 2.5–50	0.020	[34]
Fe-HHTP/PGE	BPA	Simultaneous	0.01–100	0.0008	[9]
IL/c-MWCNTs@Cu-ZIF-67/GCE	BPA	Individual	0.06–1; 1–100	0.009	This work
MIP@f-MWCNT/chitosan/GCE	BPS	Individual	1–60	2.000	[13]
CTpPa-2/GCE	BPS	Simultaneous	0.5–8; 8–50	0.090	[34]
Fe-HHTP/PGE	BPS	Simultaneous	0.01–100	0.0017	[9]
IL/c-MWCNTs@Cu-ZIF-67/GCE	BPS	Individual	0.1–2; 2–100	0.024	This work

3.6. Selectivity, Reproducibility, and Storage Stability

3.6.1. Selectivity and Interference Studies

Interference experiments were performed with BPA and BPS measured separately at 50 μM. Phenol, catechol, resorcinol, hydroquinone, and the other bisphenols were tested individually at 250 μM, which is five times the target concentration. Three measurements were made under each condition, and the responses were expressed relative to the corresponding interferent-free peak current.

Figure 11a,b present the measured oxidation peak currents in μA. Relative to the interferent-free responses, the signals were 96.42–99.33% for BPA and 91.82–98.73% for BPS, with RSDs below 1.7%. BPA at fivefold excess caused an 8.18% decrease in the BPS response, whereas BPS at fivefold excess caused a 3.2% decrease in the BPA response. These results describe the selectivity of the separate assays under the conditions examined.

3.6.2. Reproducibility and Storage Stability

The electrode-to-electrode reproducibility was evaluated using five independently prepared modified electrodes. For separate measurements of 50 μM BPA and BPS, the relative standard deviations (RSDs) of the oxidation peak currents were 3.65% and 3.30%, respectively (Figure 11d), indicating good reproducibility of electrode preparation.

The storage stability of the modified electrode was evaluated over 30 days at 4 °C using separate 50 μM BPA and BPS solutions. Relative to day 1, the BPA current retention was 96.9%, 93.8%, 90.6%, and 88.4% after 3, 7, 14, and 30 days, respectively. The corresponding values for BPS were 95.6%, 92.4%, 89.3%, and 85.6% (Figure 11c). Triplicate measurements at each time point gave RSDs of 0.63–1.52%.

3.7. Analysis of Plastic Leachates

The method was evaluated using aqueous leachates from PC drinking cups and PES baby bottles, with BPA and BPS determined in the corresponding matrices. Liquid-chromatographic screening of the original, undiluted leachates showed no detectable BPA in the PC sample or BPS in the PES sample. Neither analyte was detected by DPV in the

corresponding unspiked, fivefold-diluted matrix. After addition of known analyte concentrations, each solution was measured three times and the concentrations were calculated from the appropriate external calibration segment; the 1.0 μM BPA spike was evaluated using the low-concentration relationship. The recoveries ranged from 96.6% to 101.8% for the proposed electrochemical method, while HPLC yielded recoveries of 97.9–103.3% (Table 2), indicating generally comparable results.

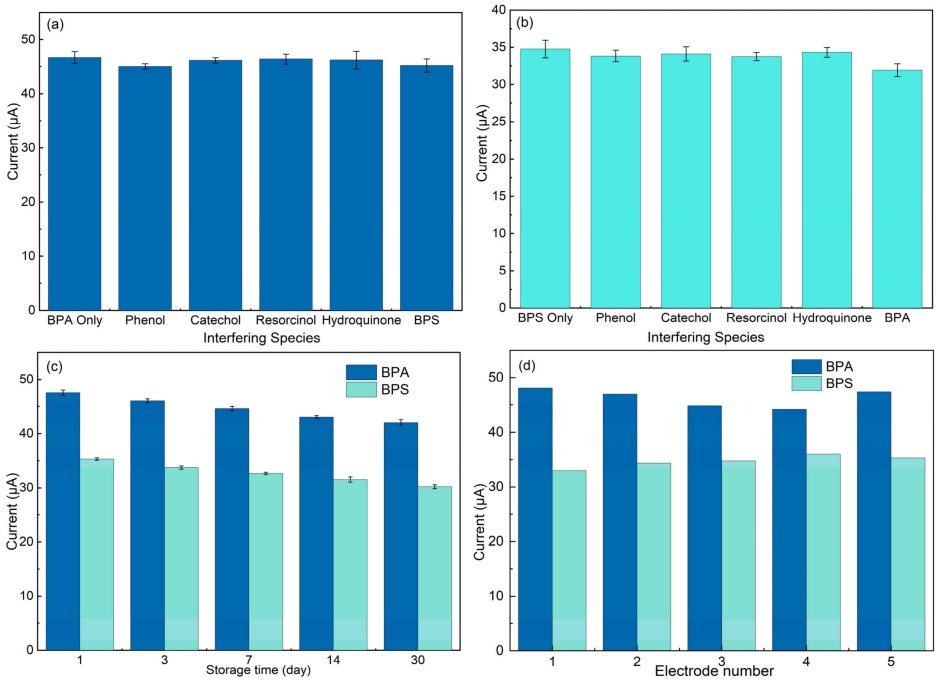


Figure 11. Selectivity, storage stability and electrode-to-electrode reproducibility of IL/c-MWCNTs@Cu-ZIF-67/GCE: anodic peak currents recorded for (**a**) 50 μM BPA and (**b**) 50 μM BPS in the presence of individual potential interferents; (**c**) BPA and BPS anodic peak currents during storage at 4 °C over 30 days; (**d**) anodic peak currents of BPA and BPS measured using five independently prepared modified electrodes. Each interferent was tested at five times the target-analyte concentration. Relative responses in the text were calculated using the corresponding analyte-only controls. Error bars in (**a**–**c**) show the reported triplicate measurement variability ($n = 3$).

Table 2. Spike-recovery results obtained using the proposed electrochemical sensor and HPLC for individually determined BPA and BPS in PC cup and PES baby-bottle leachates ($n = 3$).

Sample	Analyte	Added (μM)	IL/c-MWCNTs@Cu-ZIF-67-Modified Electrochemical Sensor			HPLC	
			Found (μM)	Recovery (%)	RSD (%)	Found (μM)	Recovery (%)
PC cup leachate	BPA	—	ND	—	—	ND	—
PC cup leachate	BPA	0.1	0.099 ± 0.003	99.0	2.9	0.099 ± 0.002	99.0
PC cup leachate	BPA	1.0	0.968 ± 0.022	96.8	2.3	1.033 ± 0.014	103.3
PC cup leachate	BPA	10	9.937 ± 0.278	99.4	2.8	9.789 ± 0.087	97.9
PES baby-bottle leachate	BPS	—	ND	—	—	ND	—
PES baby-bottle leachate	BPS	0.5	0.509 ± 0.013	101.8	2.5	0.512 ± 0.008	102.4
PES baby-bottle leachate	BPS	5.0	4.981 ± 0.079	99.6	1.6	5.013 ± 0.022	100.3
PES baby-bottle leachate	BPS	20	19.325 ± 0.232	96.6	1.2	19.87 ± 0.052	99.3

ND, not detected by the respective method in the corresponding unspiked leachate. Recovery (%) = $[(C_{found} - C_{original})/C_{added}] \times 100$, with $C_{original}$ treated as zero for the unspiked samples reported as ND. For the electrochemical method, found concentrations were calculated from each individual peak current before averaging; RSD (%) was calculated from the three corresponding back-calculated concentrations (sample standard deviation, $n = 3$).

4. Conclusions

The IL/c-MWCNTs@Cu-ZIF-67 composite was used to modify a glassy carbon electrode for the individual voltammetric determination of BPA and BPS. The modified electrode exhibited higher oxidation peak currents for both analytes than the control electrodes. The porous Cu-ZIF-67 framework provides electrochemically active sites, while c-MWCNTs form a conductive network that facilitates electron transfer. The incorporation of [BMIM][PF_6] modifies the electrode interface and favors the accumulation and oxidation of BPA and BPS. Linear calibration ranges of 0.06–1 and 1–100 μM were obtained for BPA, while BPS showed linear ranges of 0.1–2 and 2–100 μM. The LODs were 0.009 and 0.024 μM, and the estimated LOQs were 0.030 and 0.079 μM for BPA and BPS, respectively. The peak-current RSDs across five independently prepared electrodes were 3.65% for BPA and 3.30% for BPS. After storage at 4 °C for 30 days, the electrode retained 88.4% and 85.6% of its initial responses to BPA and BPS, respectively. The electrode also showed tolerance to the tested potential interferents at fivefold excess concentrations. Spike recoveries in PC drinking-cup and PES baby-bottle leachates ranged from 96.6% to 101.8%, supporting the applicability of the method to the tested aqueous leachate matrices. The same noble-metal-free sensing layer can be used for the individual determination of BPA and its substitute BPS, offering a practical option for bisphenol screening in plastic leachates.

Author Contributions: Conceptualization, F.L.; methodology, J.X. (Jing Xu); investigation, J.X. (Jing Xu); validation, W.D.; visualization, W.D.; writing—original draft preparation, J.X. (Jing Xu); writing—review and editing, J.X. (Jing Xu), W.D., W.L., X.F., Y.W., C.L. (Cong Liu), J.X. (Jun Xu), M.B., C.L. (Chunjiang Li) and F.L.; supervision, F.L.; project administration, C.L. (Chunjiang Li); funding acquisition, J.X. (Jun Xu) and M.B. All authors have read and agreed to the published version of the manuscript.

Funding: This research was funded by the Heilongjiang Provincial Key Research and Development Program (grant numbers 2025ZX05A03 and 2024ZX12C34) and the Joint Fund Cultivation Program of the Natural Science Foundation of Heilongjiang Province (grant number PL2026H210).

Institutional Review Board Statement: Not applicable.

Informed Consent Statement: Not applicable.

Data Availability Statement: The original contributions presented in this study are included in the article. Further inquiries can be directed to the corresponding author(s).

Acknowledgments: During the preparation of this manuscript, the authors used ChatGPT (OpenAI, GPT-5) for language editing, formatting, and numerical consistency checks. The authors reviewed and edited the output and take full responsibility for the content of this publication.

Conflicts of Interest: The authors declare no conflicts of interest.

References

1. Lü, L.; Liu, Y.; Yang, Y.; He, J.; Luo, L.; Chen, S.; Xing, H. Bisphenol A Exposure Interferes with Reproductive Hormones and Decreases Sperm Counts: A Systematic Review and Meta-Analysis of Epidemiological Studies. *Toxics* **2024**, *12*, 294. [CrossRef] [PubMed]
2. Xiao, T.; Huang, Z.; Zheng, C.; Quach, B.; Zhu, Y.; Li, F.; Liang, W.; Baker, J.; Reichetzeder, C.; Hocher, B.; et al. Associations of bisphenol A exposure with metabolic syndrome and its components: A systematic review and meta-analysis. *Obes. Rev.* **2024**, *25*, e13738. [CrossRef] [PubMed]
3. Stanojević, M.; Sollner Dolenc, M. Mechanisms of bisphenol A and its analogs as endocrine disruptors via nuclear receptors and related signaling pathways. *Arch. Toxicol.* **2025**, *99*, 2397–2417. [CrossRef] [PubMed]
4. Srebny, V.; Henneberger, L.; König, M.; Huchthausen, J.; Braasch, J.; Escher, B.I. Beyond Estrogenicity: A Comparative Assessment of Bisphenol A and Its Alternatives in In Vitro Assays Questions Safety of Replacements. *Environ. Sci. Technol.* **2025**, *59*, 17457–17470. [CrossRef] [PubMed]

5. Tanzer, M.; Boissiere-O'Neill, T.; Sly, P.D.; Vilcins, D. Phthalates, bisphenols and per-and polyfluoroalkyl substances migration from food packaging into food: A systematic review. *Rev. Environ. Health* **2025**, *40*, 616–625. [CrossRef] [PubMed]
6. Abbasi, F.; De-la-Torre, G.E.; KalantarHormozi, M.R.; Schmidt, T.C.; Dobaradaran, S. A review of endocrine disrupting chemicals migration from food contact materials into beverages. *Chemosphere* **2024**, *355*, 141760. [CrossRef] [PubMed]
7. Özcan, S.; Uzunoğlu, Ü.E.; Levent, S.; Can, N.Ö. A solid phase extraction of bisphenol derivatives for their LC-PDA-MS/MS determination in beverages of the Turkish market and its greenness, whiteness, and blueness assessment. *J. Food Compos. Anal.* **2024**, *136*, 106794. [CrossRef]
8. Ziyue, Z.; Qi, Z.; Shuangshuang, T.; Ziwei, Z.; Yanyu, D.; Berlin, L. Simultaneous determination of 15 bisphenols in prepared dishes by solid phase extraction purification-ultra performance liquid chromatography-tandem mass spectrometry. *Chin. J. Chromatogr.* **2025**, *43*, 1089–1099. [CrossRef] [PubMed]
9. Chen, J.-Y.; Weng, Y.-X.; Han, Y.-H.; Ye, R.-H.; Huang, D.-H. A novel pencil graphite electrode modified with an iron-based conductive metal-organic framework exhibited good ability in simultaneous sensing bisphenol A and bisphenol S. *Ecotoxicol. Environ. Saf.* **2024**, *272*, 116065. [CrossRef] [PubMed]
10. Zhang, Y.; Lei, Y.; Lu, H.; Shi, L.; Wang, P.; Ali, Z.; Li, J. Electrochemical detection of bisphenols in food: A review. *Food Chem.* **2021**, *346*, 128895. [CrossRef] [PubMed]
11. Luis-Sunga, M.; Carinelli, S.; García, G.; González-Mora, J.L.; Salazar-Carballo, P.A. Electrochemical Detection of Bisphenol A Based on Gold Nanoparticles/Multi-Walled Carbon Nanotubes: Applications on Glassy Carbon and Screen Printed Electrodes. *Sensors* **2024**, *24*, 2570. [CrossRef] [PubMed]
12. Hyder, A.; Ali, A.; Buledi, J.A.; Memon, R.; Al-Anzi, B.S.; Memon, A.A.; Kazi, M.; Solangi, A.R.; Yang, J.; Thebo, K.H. A NiO-nanostructure-based electrochemical sensor functionalized with supramolecular structures for the ultra-sensitive detection of the endocrine disruptor bisphenol S in an aquatic environment. *Phys. Chem. Chem. Phys.* **2024**, *26*, 10940–10950. [CrossRef] [PubMed]
13. Mwanza, C.; Zhao, L.; Zhang, Q.; Ding, S.-N. Electrochemical Detection of Bisphenol S Based on Molecularly Imprinted Polymers Grafted on Functionalized Multiwalled Carbon Nanotubes: A Facile Sensor Fabrication Approach. *Chemosensors* **2025**, *13*, 236. [CrossRef]
14. Liu, C.; Sun, Y.; Chang, S.; Jin, J.; Hu, J.; Zhao, J. An Electrochemical Sensor for the Detection of Bisphenols Based on Mxene Embedded with Aminated Carbon Nanotubes. *Electroanalysis* **2025**, *37*, e70028. [CrossRef]
15. Wang, L.; Hong, Q.; Zhao, L.; Wang, D.; Zhi, K. Novel crown ether-based covalent organic frameworks with dual binding sites for metal-free electrochemical sensors detecting bisphenol A. *Microchem. J.* **2025**, *214*, 114044. [CrossRef]
16. Tien, N.N.; Dat, N.T.; Manh, N.B.; Ngan, N.T.T.; Osial, M.; Pisarek, M.; Chernyayeva, O.; Thu, V.T. A simple one-pot approach to prepare composites based on bimetallic metal–organic frameworks M, Ni-BTC (M = Cu, Fe) and carbon nanotubes for electrochemical detection of bisphenol A. *J. Nanoparticle Res.* **2025**, *27*, 87. [CrossRef]
17. Nandhini, C.; Huang, C.-H.; Mani, G.; Arul, P.; Huang, S.-T. Development of ternary hybrid composites of transition metal and noble metal-based heterostructures: Ultrasensitive simultaneous electrochemical detection of bisphenol A and bisphenol S in food samples. *Food Chem.* **2024**, *459*, 140451. [CrossRef] [PubMed]
18. Lin, Q.; Lin, G.; Dai, L.; Huang, D.; Huang, X. Simultaneous Detection of Bisphenol A and Bisphenol S Migration in Food-Contact Plastics Based on a Dual-ligand Metal-organic Framework. *Sci. Technol. Food Ind.* **2025**, *46*, 251–259. [CrossRef]
19. Atkare, S.; Jagtap, S.; Late, D.J. Exploring the potential of metal–organic framework based composites as key players in bisphenol detection. *Chem. Soc. Rev.* **2025**, *54*, 3736–3774. [CrossRef] [PubMed]
20. Garcia-Rodrigo, L.; Tortolini, C.; González-Cortés, A.; Ventura, I.; Migliaccio, S.; Ferretti, E.; Antiochia, R. A simple MOF-based nanosensor for bisphenol A detection: In vitro application in supernatant of human endothelial cell models. *Biosens. Bioelectron. X* **2025**, *26*, 100666. [CrossRef]
21. Xie, Y.; Yin, J.; Zhou, W.; Wang, L.; Deng, F.; Yi, X.; Guo, Q.; Salminen, K.; Sun, J.; Liu, L. ZIF-8@aminopropyl-functionalized magnesium phyllosilicate/carbon nanotubes composite for sensitive electrochemical detection of bisphenol A in real samples. *Mater. Sci. Semicond. Process.* **2025**, *194*, 109594. [CrossRef]
22. Hu, Y.; Wei, Z.; Li, W.; Wang, X.; Yang, H. One-step green synthesis of flower-like non-precious metal (Cu, Ni, Fe or Zn) doped ZIF-67 and its application as non-enzymatic electrochemical glucose sensors. *Int. J. Electrochem. Sci.* **2024**, *19*, 100736. [CrossRef]
23. Nakahara, H.; Hitomi, Y. Designing Artificial Laccase Catalysts by Introducing Substrate Oxidation Metals into Oxygen-Reducing Metal-Organic Frameworks: Cu-Doped ZIF-67. *Chem. A Eur. J.* **2024**, *30*, e202402953. [CrossRef] [PubMed]
24. Wulandari, C.; Muslihati, A.; Septiani, N.L.W.; Nuruddin, A.; Yuliarto, B.; Yamauchi, Y.; Henzie, J.; Peiner, E.; Wasisto, H.S.; Nugraha, N. Carbon-black-coupled bimetallic CoCu-ZIF composites for monohydroxylated polycyclic aromatic hydrocarbon metabolite sensing. *Commun. Mater.* **2026**, *7*, 195. [CrossRef]
25. Beitollahi, H.; Garkani Nejad, F.; Dourandish, Z.; Zaimbashi, R.; Tajik, S.; Adeloju, S. Electrochemical sensor based on ZIF-67/MWCNTs nanocomposite for 4-aminophenol determination in water samples. *Appl. Water Sci.* **2026**, *16*, 58. [CrossRef]

26. Shahid, Z.; Fu, B.; Rehman, S.; Ahmad, Z.; Chen, J.; Lu, X. Potential-resolved real-time ultrasensitive sensing of bisphenol compounds based on ionic liquid coupled Zr-MOF@GO nanosensor. *Microchem. J.* **2024**, *207*, 111888. [CrossRef]
27. Zhang, L.; Han, Y.; Sun, M.; Li, S. Non-enzymatic electrochemical sensor based on ionic liquid [BMIM][PF_6] functionalized zirconium-copper bimetallic MOF composite for the detection of nitrite in food samples. *Food Chem.* **2024**, *456*, 140023. [CrossRef] [PubMed]
28. Gorenskaia, E.; Uzice, S.; Jalali, M.; Fuller, R.O.; Mecerreyes, D.; Silvester, D.S. Anti-fouling properties of an ionic liquid/poly(ionic liquid) gelled electrolyte for the electrochemical detection of bisphenol A. *Electrochim. Acta* **2026**, *563*, 148712. [CrossRef]
29. Beduk, T.; Gomes, M.; De Oliveira Filho, J.I.; Shetty, S.S.; Khushaim, W.; Garcia-Ramirez, R.; Durmus, C.; Ait Lahcen, A.; Salama, K.N. A Portable Molecularly Imprinted Sensor for On-Site and Wireless Environmental Bisphenol A Monitoring. *Front. Chem.* **2022**, *10*, 833899. [CrossRef] [PubMed]
30. Chen, Q.; Yuan, C.; Zhai, C. Label-free photoelectrochemical sensor based on 2D/2D $ZnIn_2S_4$/g-C_3N_4 heterojunction for the efficient and sensitive detection of bisphenol A. *Chin. Chem. Lett.* **2022**, *33*, 983–986. [CrossRef]
31. Lin, F.; Geng, J.; Lv, Y.; Huang, Z.; Scherman, D.; He, S.; Li, H.; Sun, T.; Sun, W. Pt@COOH-MWCNT enhanced conductive hydrogel with antibacterial and salt-tolerant properties for sensitive electrochemical detection of bisphenol A in seawater. *Microchem. J.* **2026**, *230*, 119703. [CrossRef]
32. Gibi, C.; Anandan, S.; Liu, C.-H.; Wu, J.J. Sensitive electrochemical detection of bisphenol A in aqueous samples using $CuWO_4$/f-MWCNT nanocomposites. *Microchem. J.* **2025**, *213*, 113822. [CrossRef]
33. Soylemez, M.S.; Bas, S.Z.; Sarilmaz, A.; Özel, F.; Özmen, M. Electrochemical detection of bisphenol A in water samples through a ternary nanocomposite-based laboratory-made sensing platform. *J. Environ. Chem. Eng.* **2025**, *13*, 117856. [CrossRef]
34. Pang, Y.-H.; Huang, Y.-Y.; Wang, L.; Shen, X.-F.; Wang, Y.-Y. Determination of bisphenol A and bisphenol S by a covalent organic framework electrochemical sensor. *Environ. Pollut.* **2020**, *263*, 114616. [CrossRef]

Disclaimer/Publisher's Note: The statements, opinions and data contained in all publications are solely those of the individual author(s) and contributor(s) and not of MDPI and/or the editor(s). MDPI and/or the editor(s) disclaim responsibility for any injury to people or property resulting from any ideas, methods, instructions or products referred to in the content.